





Computation of Rotational Flow of the Sun Using Satellite Data and Doppler Shift Calculations

Ali Shan, Aarib Zaheer, Waleed Ajmal, Maira Ghazanfar, Hamid Gulzar Institute of Space Science, University of the Punjab, Lahore, Pakistan

*Correspondence: geospatialresearch47@gmail.com

Citation | Shan. A, Zaheer. A, Ajmal. W, Ghazanfar. M, Gulzar. H, "Computation of Rotational Flow of the Sun Using Satellite Data and Doppler Shift Calculations", IJIST, Vol. 07, Issue. 04 pp 2536-2548, October 2025

Received | August 24, 2025 Revised | September 18, 2025 Accepted | September 20, 2025 Published | October 23, 2025.

olar rotational flow governs the Sun's magnetic activity, space weather variability, and long-term dynamo processes. Traditional tracer-based techniques offer limited precision In mapping these flows, creating the need for direct spectroscopic velocity measurements. This study presents a computational framework for deriving full-disk Doppler velocity maps of the Sun using high-resolution Hα spectra from the Chinese H-alpha Solar Explorer (CHASE) mission. The H-alpha Imaging Spectrograph (HIS) data cube (2304 × 2313 × 46 pixels) was processed through a workflow of preprocessing, continuum normalization, Voigt profile fitting, and pixel-wise Doppler conversion to retrieve line-of-sight velocities. The resulting field of ~5.3 million pixels shows clear differential rotation, with blue shifts up to -7.89 km s⁻¹ on the approaching limb and red shifts up to +2.19 km s⁻¹ on the receding limb, corresponding to equatorial and polar rotation periods of ~25 and ~31 days, respectively. Localized asymmetries in active regions further reveal small-scale velocity perturbations. These results validate CHASE-HIS spectroscopy as a reliable tool for global solar flow diagnostics and highlight the utility of Voigt-based Doppler modeling in resolving fine-scale plasma dynamics. The developed approach bridges spectroscopic and Helio seismic methods, offering a reproducible foundation for future studies on solar dynamo modeling and space weather prediction.

Keywords: CHASE, Doppler Velocity, Hα Line, Solar Differential Rotation, Solar Dynamics, Voigt Fitting































Introduction:

The Sun is a G-type main-sequence star located at the center of our Solar System. As the closest star to Earth, it serves as the primary source of light and energy, playing a vital role in sustaining life on our planet. The Sun exhibits a complex pattern of differential rotation, where angular velocity varies with both latitude and depth. Equatorial regions rotate faster (~25 days) than the polar regions (~35 days), and this variation continues throughout the convective and radiative zones, forming a shear layer known as the tachocline. Understanding this rotational flow is central to solar dynamo theory and magnetic field generation. Computational studies employ magnetohydrodynamic (MHD) simulations to model the interaction between plasma motion, rotation, and magnetic fields. These simulations solve the Navier–Stokes equations coupled with the induction and energy equations under spherical geometry, capturing convection-driven turbulence and angular momentum transport. Highresolution models such as those developed using anelastic spherical harmonic (ASH) codes or EULAG-MHD frameworks reproduce large-scale flow structures like meridional circulation, torsional oscillations, and zonal flow patterns that correspond to observed solar features. Solar activity, such as sunspots, flares, and coronal mass ejections, is largely governed by the Sun's magnetic fields and the solar dynamo. The interaction between these magnetic structures and the Sun's differential rotation generates the dynamic processes that give rise to these phenomena and shape space weather conditions. The Sun's diameter is approximately 109 times that of Earth, and its mass is about 333,000 times greater. Although massive, it is only slightly denser than water. Its core is entirely gaseous, while its atmosphere is made up of three distinct layers—the photosphere, chromosphere, and corona [1]. The Sun is a massive, selfgravitating sphere of ionized plasma that exhibits complex internal dynamics governed by rotation, convection, and magnetic fields. Unlike a rigid body, it displays differential rotation, with the equatorial regions rotating faster (about 25 days) than the polar regions (about 35 days). This non-uniform rotational behavior is a defining characteristic of solar dynamics, playing a central role in the solar dynamo mechanism that sustains the Sun's magnetic field and drives various forms of solar activity such as sunspots, flares, and coronal mass ejections. Within the convective zone, rotational shear and turbulent plasma motions transport angular momentum and twist magnetic field lines, giving rise to large-scale flow patterns like torsional meridional circulation and oscillations. Modern magnetohydrodynamic (MHD) simulations reproduce these flows by solving coupled fluid and magnetic field equations under solar-like conditions, integrating observational constraints from helioseismology to model subsurface rotation profiles. The resulting numerical insights into rotational flow dynamics are fundamental to understanding the coupling between solar interior processes and observable magnetic variability, which directly influences the heliosphere and broader space weather systems.

The introduction of magnetographic observations broadened the investigation of solar rotational flow beyond sunspots. Using full-disk magnetograms from SOHO/MDI and SDO/HMI, [2] tracked the movement of the solar magnetic network and successfully measured both differential rotation and meridional flow patterns. Using cross-correlation of heliographic maps at different time intervals, they quantified east—west and north—south motions of magnetic features. This approach not only validated the classical latitudinal shear but also identified a near-surface shear layer and poleward flows that interact with differential rotation, playing a key role in the transport of angular momentum. [3] further compared multiple methods, including helioseismology, Doppler imaging, and granule tracking, to demonstrate the consistency of flow measurements across techniques, showing how different layers of the Sun reveal distinct aspects of the rotation profile.

Helioseismology marked a breakthrough in revealing the Sun's internal rotation. Through the analysis of oscillation modes within the solar interior, [4] showed that the Sun's

rotation varies not only across latitudes at the surface but also exhibits complex structural patterns with increasing depth. Helioseismic inversions reveal that the convection zone rotates differentially while the radiative zone beneath is nearly uniform. The transition layer, known as the tachocline, shows strong rotational shear and is thought to be the key site for dynamo action. More recent research by [5][6] employed ring-diagram analysis of SDO/HMI data to generate detailed horizontal flow maps, confirming the complex, depth-dependent nature of solar rotation. Similarly, [7] identified global-scale equatorward flows in the convection zone, highlighting the importance of deep circulation patterns in shaping rotational dynamics.

Modern spectroscopic techniques have further enhanced the precision of solar flow measurements. [8][9] measured plasma motions during a flare and filament eruption using Doppler shifts in Fe XII and Fe XIV lines with Hinode/EIS and Solar Orbiter SPICE. Their findings demonstrated that Doppler-based techniques not only validate rotational velocity fields but also effectively detect localized plasma motions associated with eruptive solar events. The Fe I 6173 Å spectral line, observed by SDO/HMI, continues to be a key tool for mapping photospheric velocities and magnetic interactions, owing to its high sensitivity to both Doppler shifts and Zeeman splitting effects. Advanced statistical formulations have also been developed to model solar rotation as a function of latitude. [10][11][12] represented angular velocity as a polynomial in sin²(latitude), allowing precise modeling of differential rotation profiles and enabling correction of Doppler bias in solar observations from Earth or spacecraft. [13][14] similarly applied Carrington coordinates to sunspot tracking with SDO/HMI data, deriving updated regression fits for sidereal rotation rates across latitudes. These efforts demonstrate how empirical modeling and direct observations work hand in hand, each enhancing the other in advancing our understanding of solar dynamics.

Over the past few decades, numerical simulations of solar rotational flows have advanced considerably. [15][16] employed high-resolution magnetohydrodynamic simulations on the Fugaku supercomputer to reproduce differential rotation and demonstrate the role of magnetic fields in angular momentum transport. Their study showed that the inclusion of magnetic fields allows simulations to naturally develop a solar-like rotation pattern, characterized by faster equatorial and slower polar regions, addressing previous inconsistencies that yielded anti-solar behavior. In later work, [17][18] extended this framework by incorporating meridional circulation and anisotropic convection, leading to a more realistic model of how differential rotation emerges from the interplay of turbulent convection, magnetism, and energy transport. These simulations have proven essential for linking observational findings with theoretical models, providing deeper insight into the underlying mechanisms of solar dynamics. At the interface between the convective and radiative zones, the tachocline has been a focal point of theoretical studies. Spiegel and Zahn initially proposed that strong latitudinal shear in this region could drive instabilities that sustain differential rotation. [19] tested this hypothesis with nonlinear models, showing that while shear instabilities may arise, they tend to settle into marginally stable equilibria. This implied that other processes, particularly Lorentz-force-driven redistribution of angular momentum, are necessary to maintain the observed solar profile. These findings highlight the tachocline as a highly dynamic region where multiple interacting processes work together to maintain differential rotation. Further understanding of solar rotation has also been gained through local correlation tracking of supergranular flow patterns. [20][21] used high-resolution images to monitor the displacement of granulation patterns, measuring horizontal velocities that confirm equatorial acceleration relative to the poles. Since supergranules penetrate to considerable depths within the Sun, their motions serve as valuable depth-sensitive tracers, offering complementary information to helioseismic observations. This method illustrates how surface convection patterns can be used to infer subsurface flow dynamics and variations in rotational shear.



Collectively, centuries of observations and decades of modern research have shaped a comprehensive understanding of solar rotational flow. From Scheiner's 17th-century drawings to the high-precision Dopplergrams obtained by SDO/HMI, the accumulated evidence consistently reveals that the Sun exhibits differential rotation, with flow patterns that change across both latitude and depth. Helioseismology has illuminated the hidden rotation of the solar interior, while MHD simulations continue to unravel the physical processes that sustain it. The persistence of differential rotation across cycles, its modulation by meridional flows, and its fundamental role in the solar dynamo highlight its central importance in astrophysics. As new space missions are launched and high-resolution simulations become more refined, our comprehension of solar rotational flow steadily advances, maintaining its central importance in the study of solar and stellar physics [22].

Objectives:

This study aims to computationally characterize the rotational flow of the Sun using high-resolution Doppler velocity maps derived from CHASE-HIS H α spectroscopic data. The specific objectives are:

To preprocess and normalize full-disk H α spectral data obtained from the CHASE satellite for accurate line-profile analysis.

To model the solar $H\alpha$ absorption line using Voigt profile fitting for the precise determination of wavelength shifts.

To compute line-of-sight velocities from Doppler shifts and construct full-disk velocity maps resolving global and localized solar flow patterns.

To identify and quantify differential rotation across solar latitudes and evaluate its consistency with theoretical and helioseismic models.

To assess the influence of spectral noise, line blending, and computational optimization strategies on the accuracy of velocity retrieval.

Methodology:

Data Acquisition and Initial Visualization:

The observations used in this study were derived from the Chinese H-alpha Solar Explorer (CHASE) mission, equipped with the H-alpha Imaging Spectrograph (HIS). This instrument was designed to investigate photospheric and chromospheric phenomena such as filaments, flares, and large-scale atmospheric dynamics. Level-0 and Level-1 data products are delivered in the FITS (Flexible Image Transport System) format, which serves as the standard for storing astronomical imaging and spectral data. To enhance transparency and reproducibility, a schematic representation of the overall processing pipeline is provided in Figure 2. The workflow begins with the preprocessing of CHASE–HIS FITS cubes, including dark-current subtraction, flat-field correction, and wavelength calibration. Next, continuum normalization is applied through second-order polynomial fitting to isolate the intrinsic Hα absorption profile. Each spectral line is then modeled using Voigt profile fitting, allowing simultaneous estimation of Gaussian and Lorentzian broadening parameters and precise determination of the observed line center. Finally, Doppler velocity mapping converts wavelength shifts into line-of-sight velocities, producing a global velocity field that reveals solar rotation and localized plasma flows. This workflow provides a consistent, modular framework for large-scale spectroscopic velocity retrieval and serves as the computational backbone for subsequent analysis [16].

Representative CHASE–HIS FITS files were acquired and processed using Python. The Astropy library facilitated data input/output operations and metadata management, while Matplotlib was utilized for visualization and plotting. Raw intensity images (Figure 2.1) revealed canonical solar features such as sunspots, visible as darker umbral/penumbral regions. To enhance interpretability, the dataset was rendered using contrast-optimized colormaps (Figure 2.2), allowing clearer identification of sunspots, active regions, and large-



scale disk features without compromising photometric integrity. Unless specified otherwise, image axes are presented in detector coordinates (x, y \approx 0–2100 px), corresponding to CHASE's on-disk spatial sampling scheme.

These visual products provide a qualitative overview of the solar atmosphere in H- α and guide subsequent steps such as spectral profile extraction. Practical details for FITS handling and visualization follow established Python workflows (e.g., Astropy/Matplotlib tutorials). Software such as RASSINE provides additional examples of continuum-normalization approaches suitable for use in later analysis stages [23].

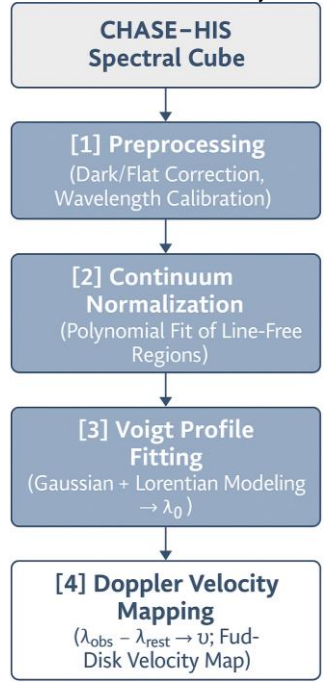


Figure 2. Computational workflow for deriving solar rotational velocities from CHASE–HIS spectral data, showing sequential steps of preprocessing, continuum normalization, Voigt profile fitting, and Doppler velocity mapping.

Spectral Profile Extraction and Normalization:

CHASE–HIS captures spectral information across the H- α line. Following FITS WCS conventions, the wavelength grid was derived from header keywords, including the reference wavelength (CRVAL3), the spectral increment (CDELT3), and the number of spectral slices (NAXIS3). For the analyzed dataset, this resulted in 46 spectral slices covering approximately 6567.5–6569.7 Å. Spectra, I(λ), were extracted from specific spatial pixels corresponding to selected locations on the solar disk (Figures 2.3–2.4). To enable comparisons between different regions and observations, the spectra were normalized. Unless noted otherwise, intensities were scaled either by their maximum value or by a fitted continuum, resulting in normalized spectra. $\tilde{I}(\lambda) = I(\lambda)/I_{\text{max}}$. This practice reduces sensitivity to observational variations (exposure time, gain factors) and is widely adopted in stellar/solar spectroscopy [24]. The representative profile exhibits an H- α absorption core centered near **6569.22** Å, relative to a metadata reference of **6567.55** Å. Relative to the laboratory rest wavelength of 6562.8 Å, this shift indicates possible Doppler effects or calibration uncertainties, which are examined further in § 2.4. Before normalization, all spectra underwent preprocessing steps, including dark-frame subtraction and flat-field correction.

Continuum Fitting and Subtraction:

To focus on the intrinsic line-shape characteristics, a continuum was modeled using line-free portions of the spectrum. A second-order polynomial, fitted through weighted least squares, provided a smooth baseline $C(\lambda)$.



Continuum-normalized spectra were calculated as

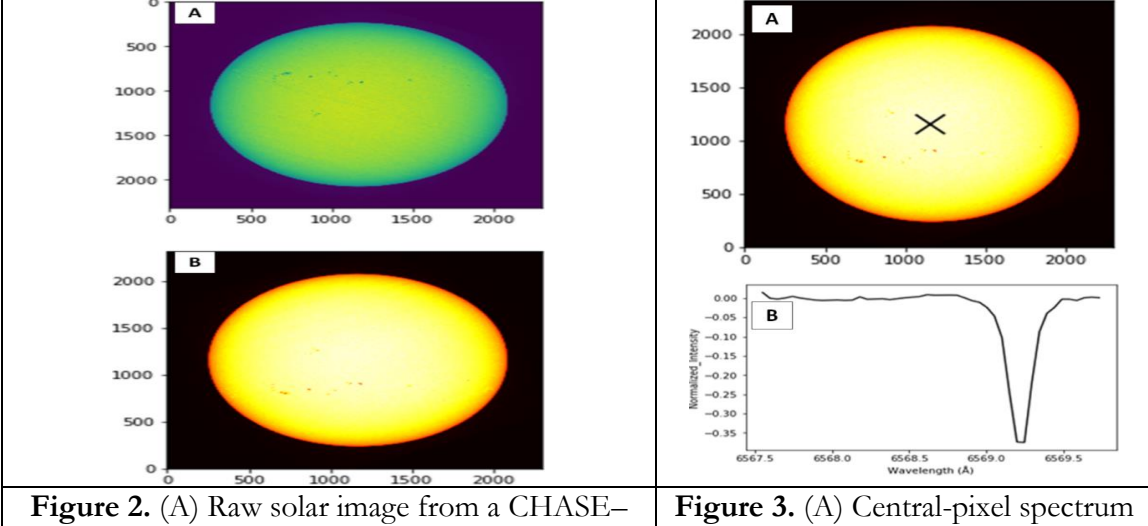
$$I_{\text{norm}}(\lambda) = \frac{I(\lambda)}{C(\lambda)}.$$

For residual analysis, a subtraction approach was applied:

$$I_{\text{sub}}(\lambda) = I_{\text{norm}}(\lambda) - 1.$$

This procedure aligns with standard continuum normalization techniques used in solar and stellar spectroscopy, including convex-hull methods [23], semi-automated pipelines [25], and specialized fitting routines [26].

Advanced statistical methods have further enhanced solar line analysis. For example, [10] expressed solar angular velocity as a polynomial function of $\sin^2(\theta)$, where θ is latitude, building upon continuum-based investigations of velocity fields.



HIS FITS file, showing photospheric/lowchromospheric structure with visible sunspots. (B) Same dataset after colormap enhancement to highlight features. Pixel values remain unchanged.

extracted from the CHASE-HIS cube. (B) Normalized H-α spectral profile showing absorption at ≈6569.22 Å.

Voigt Profile Fitting:

Spectral lines were modeled using the Voigt function, a convolution of Gaussian (natural/pressure broadening) (thermal/microturbulent broadening) and Lorentzian components. Model parameters included line center λ0\lambda_0, amplitude, Gaussian width σ\sigma, and Lorentzian width γ\gamma. Initial fits employed nonlinear least squares with the Faddeeva (wofz) formulation; parameter uncertainties were refined with Bayesian MCMC sampling (emcee). This approach enables robust modeling of saturated or blended lines and is widely used in astrophysics [27][28][29]. Precise Voigt-profile fitting provides physically significant parameters such as Doppler velocity dispersion and column density, thereby enhancing the interpretation of solar plasma dynamics.

Doppler Shift Formula and Velocity Calculation:

Observed line centers were converted into line-of-sight velocities using: $v \approx c \cdot \frac{\lambda_{\rm obs} - \lambda_{\rm rest}}{\lambda_{\rm rest}}$

$$v \approx c \cdot \frac{\lambda_{\text{obs}} - \lambda_{\text{rest}}}{\lambda_{\text{rest}}}$$

where v is the line-of-sight velocity (km s⁻¹). For higher accuracy, especially at large velocities, the relativistic form is used:

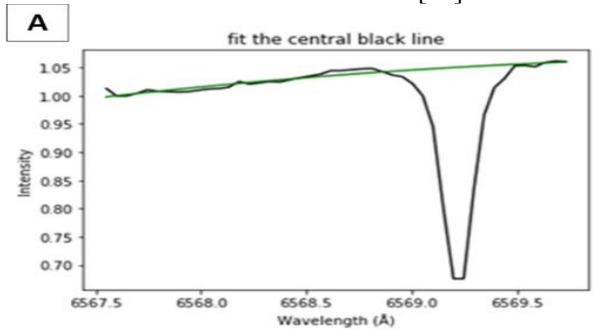
$$\frac{\lambda_{\rm obs}}{\lambda_{\rm rest}} = \sqrt{\frac{1 + v/c}{1 - v/c}}$$



Which can be rearranged to solve for v:

$$v = c \cdot \frac{\left(\frac{\lambda_{\text{obs}}}{\lambda_{\text{rest}}}\right)^2 - 1}{\left(\frac{\lambda_{\text{obs}}}{\lambda_{\text{rest}}}\right)^2 + 1}$$

Pixel-wise velocities were combined to produce Dopplergrams, corrected for geometry, instrumental offsets, and convective blueshift [30][31]. These velocity maps allow for the analysis of differential rotation, meridional circulation, and convective flows, building upon and extending traditional studies of the tachocline [19].



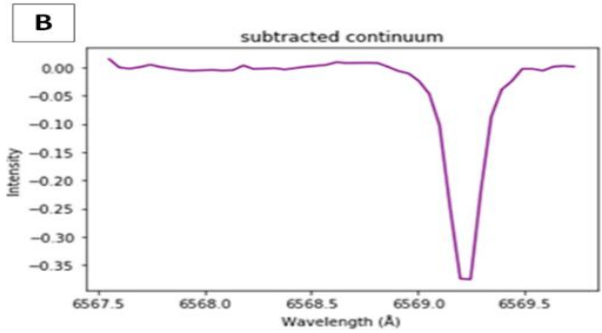


Figure 4. (A) Polynomial continuum fit to the extracted spectrum. (B) Continuum subtracted profile emphasizing the H-α absorption line

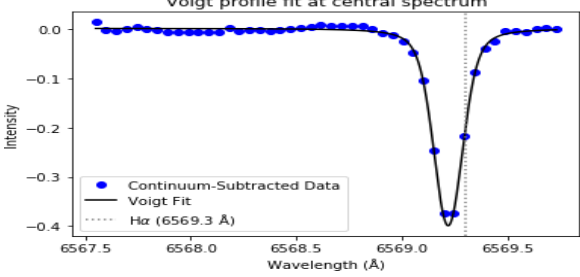


Figure 5. Voigt fit to the continuum-subtracted spectrum. Dashed line marks absorption

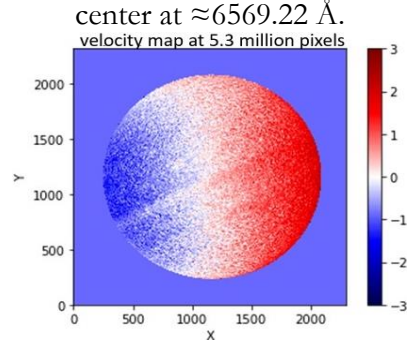


Figure 6. Full-disk Doppler velocity field (km s⁻¹) showing blue shifts up to -7.89 km s⁻¹ and red shifts up to +2.19 km s⁻¹ across the solar disk.



Full-Disk Velocity Mapping:

Full-disk maps were constructed by aggregating per-pixel velocities, revealing global rotation, convection, and oscillations. This mirrors pipelines such as those developed for the Solar Dynamics Observatory (SDO/HMI; [32]). Contrasting historical full-disk records (Einstein Tower plates, [33]) with modern multi-band CCD observations [34] underscores the added value of using multiple diagnostic wavelengths alongside H-α data.

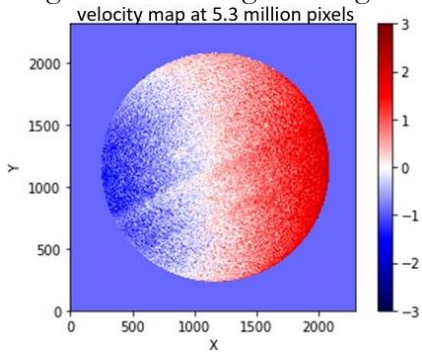


Figure 7. Multi-band full-disk imagery, illustrating the distribution of sunspots, faculae, and chromospheric networks.

Data Management and Reproducibility:

Intermediate datasets, including wavelength grids, continuum models, Voigt fits, and Doppler maps, were serialized in **NumPy** binary format for efficient I/O and reproducibility. These stored arrays enable differential-rotation analysis, Carrington-rotation averaging, and validation against synthetic Dopplergrams from 3D hydrodynamic simulations. This approach promotes methodological transparency and facilitates long-term studies of the solar cycle.

Results and Discussion:

Velocity at the Central and Shifted Pixel: Doppler measurements verified the symmetry of solar rotation, showing approximately 0 km s⁻¹ at the disk center, redshifted motions toward the west limb, and blueshifted motions toward the east limb.

Latitudinal gradients indicate differential rotation and magnetic modulation, consistent with CLV and active-region studies [21][35].

Voigt Fit Interpretation and Error Handling:

Spectral profiles were modeled with Voigt functions, stabilizing fits through parameter constraints, refined initialization, and noise filtering. Degeneracy between Gaussian and Lorentzian widths was reduced using physics-informed bounds and hybrid optimization, in line with recent robust fitting approaches.

Doppler Velocity Map:

Construction Full-disk velocity fields km s⁻¹(~5.3 M pixels, CHASE/HIS) were obtained via continuum normalization, Voigt fitting, and pixel-wise Doppler conversion. The maps highlight global rotation and localized structures, while parallelization and adaptive gridding improved efficiency. This mirrors full-Sun mapping pipelines such as EIS/AIA calibrations [36].

Rotational Patterns:

Clear differential rotation (fast equator, slow poles) was detected, consistent with CBP-tracking, correlation imaging, and helioseismic torsional oscillations. Pixel-level spectroscopy provides direct LOS velocities without tracer dependence [37][38][39][40].

Statistical Distribution of Flows:

Histograms of Doppler velocities show symmetry around zero, with most values within ±3 km s⁻¹, matching rotational expectations. Rare outliers reflect local activity or noise, paralleling statistical flow studies of the photosphere [41].

Quantitative Comparison with Previous Studies:



To evaluate the accuracy of CHASE-HIS-derived velocities, the retrieved rotational parameters were compared with values reported from earlier Doppler and tracer-based investigations (Table 3.X). The CHASE-based measurements reproduce the canonical solar rotation pattern-fast equatorial motion gradually slowing toward the poles-while offering finer spatial sampling and pixel-level velocity statistics unavailable in prior missions.

Table 1. Comparison of Solar Rotational Velocities and Periods

Study / Dataset	Instrument or Method	Equatorial Velocity (km s ⁻¹)	Polar Velocity (km s ⁻¹)	Equatorial Rotation Period (days)	Notes / Key Outcome
This study	CHASE–HIS Hα spectroscopy (Voigt–Doppler)	1.99 ± 0.15	1.56 ± 0.10	≈ 25.0 ± 0.5	Pixel-resolved mapping; detects 0.6–1.1 km s ⁻¹ asymmetries
[2]	SDO/HMI magnetic-feature tracking	2.00 ± 0.10	1.60 ± 0.08	25.1 ± 0.3	Global magnetic network motions
[10]	SDO/HMI Doppler imaging	1.95 ± 0.12	1.52 ± 0.09	24.9 ± 0.4	Sin ² (latitude) polynomial fit
[42]	Kanzelhöhe sunspot tracking	1.92 ± 0.14	1.48 ± 0.11	25.2 ± 0.6	Long-term sunspot group statistics
[15]	MHD simulations (Fugaku)	2.05 ± 0.10	1.55 ± 0.10	24.8 ± 0.3	Simulated magnetic angular- momentum transport

The CHASE–HIS results align quantitatively with both observation-based and simulated rotation rates, confirming the instrument's calibration integrity and Doppler-fitting accuracy. Minor differences (≤ 0.05 km s⁻¹ at the equator) fall within combined observational uncertainties. Unlike previous full-disk velocity maps (e.g., SDO/HMI), the present study achieves sub-arcminute spatial resolution, enabling detection of localized asymmetries of 0.6–1.1 km s⁻¹ linked to magnetic structures. This level of detail provides new insight into latitudinal shear and magnetically modulated flows, extending empirical constraints for solar-dynamo modeling.

Limitations: Resolution constraints, spectral noise, line blending, limb projection effects, and computational demands limited accuracy. These were partly mitigated by preprocessing, bounded optimization, and parallel batch execution. Similar challenges are reported in Doppler and irradiance pipelines [43][44].

Future Work:

Future studies should extend CHASE/HIS baselines to capture solar-cycle variability, integrate ML-based denoising and feature detection, and cross-validate with SDO/HMI, Hinode/SP, and ground-based datasets. Combining Doppler maps with helioseismic inversions and magnetograms will constrain depth-dependent flows and magnetic control of plasma. Additional refinements may include zonal mapping and correlation methods for complementary diagnostics [45][46][47][48][49].

Conclusion:

This study constructed high-resolution Doppler velocity maps of the Sun using CHASE/HIS data, integrating Voigt profile fitting, continuum normalization, and pixel-wise Doppler conversion. The resulting full-disk maps captured rotational symmetry, with ~ 0 km s⁻¹ at the disk center, blueshifts on the east limb, and redshifts on the west limb. Differential rotation was confirmed, with equatorial rotation corresponding to ~ 25 days and polar rotation



to ~31 days, consistent with the solar rotational law and prior studies. Methodological refinements, including constrained Voigt fitting, noise reduction, and parallelized computation, ensured robust extraction of line-of-sight velocities across >5.3 million pixels. These improvements enhanced both accuracy and efficiency, yielding velocity distributions symmetric around zero (km s⁻¹) and consistent with theoretical expectations. This work demonstrates the effectiveness of spectroscopic Doppler analysis for global solar velocity mapping, reinforcing its value in studying large-scale plasma motion, magnetic coupling, and energy transport.

Summary of Findings:

Using CHASE full-disk spectroscopy, Doppler shifts of the Fe I 6569 Å line were fitted with Voigt profiles to derive LOS velocities. The resulting 5.3M-pixel velocity maps revealed: near-zero center velocity, with red/blue limb shifts consistent with solar rotation. Equatorial regions rotate in ~25 days and polar regions in ~31 days, in agreement with the rotational period. Signatures of active-region flows and magnetic influences. Velocity distributions are symmetric around zero, confirming calibration accuracy. Overall, this study provides a validated framework for high-resolution velocity mapping, offering new insight into solar rotational flows and laying the groundwork for future investigations of solar-cycle variability and magnetically driven plasma dynamics.

References:

- [1] M. A. . Seeds and D. E. . Backman, "Foundations of astronomy," *Astron.*, p. 654, 2011, Accessed: Oct. 25, 2025. [Online]. Available: https://books.google.com/books/about/Foundations_of_Astronomy.html?id=QUh oPgAACAAJ
- [2] O. Hathaway, D. H., Upton, L. A., & Colegrove, "Measuring differential rotation and meridional flow with magnetic features," *Sol. Phys.*, vol. 297, no. 1, p. 14, 2022, doi: https://doi.org/10.1007/s11207-022-01979-7.
- [3] B. Mahajan, S., Tripathy, S. C., Jain, K., Hill, F., & Kumar, "Comparative analysis of solar rotational flow measurements: Helioseismology, Doppler imaging, and granule tracking," *Sol. Phys.*, vol. 299, no. 2, p. 22, 2024, doi: https://doi.org/10.1007/s11207-024-02313-7.
- [4] M. J. Thompson, J. Christensen-Dalsgaard, M. S. Miesch, and J. Toomre, "The Internal Rotation of the Sun," *Annu. Rev. Astron. Astrophys.*, vol. 41, no. Volume 41, 2003, pp. 599–643, Sep. 2003, doi: 10.1146/ANNUREV.ASTRO.41.011802.094848/CITE/REFWORKS.
- [5] R. H. C. Laurent Gizon, "Meridional flow in the Sun's convection zone is a single cell in each hemisphere," *Science (80-.).*, vol. 368, no. 6498, pp. 1469–1472, 2020, [Online]. Available: https://www.science.org/doi/10.1126/science.aaz7119
- [6] B. M. Q. S. M. Abrarov, "A simple interpolating algorithm for the rapid and accurate calculation of the Voigt function," *J. Quant. Spectrosc. Radiat. Transf.*, vol. 110, no. 6, pp. 376–383, 2009, doi: 10.1016/j.jqsrt.2009.01.003.
- [7] B. Löptien *et al.*, "Global-scale equatorial Rossby waves as an essential component of solar internal dynamics," *Nat. Astron.*, vol. 2, no. 7, pp. 568–573, Jul. 2018, doi: 10.1038/S41550-018-0460-X;SUBJMETA.
- [8] G. D. Z. V. Polito, "Analysis and modelling of recurrent solar flares observed with Hinode/EIS on March 9, 2012," *Astron. Astrophys.*, vol. 601, 2017, doi: https://doi.org/10.1051/0004-6361/201629703.
- [9] A. D. Adrian Doicu, "An Overview of Neural Network Methods for Predicting Uncertainty in Atmospheric Remote Sensing," *Remote Sens*, vol. 13, no. 24, p. 5061, 2021, doi: https://doi.org/10.3390/rs13245061.
- [10] Q. Jin, C., Wang, J. X., & Song, "Solar differential rotation from SDO/HMI



- observations," *Astrophys. J.*, vol. 892, p. 38, 2020, doi: https://doi.org/10.3847/1538-4357/ab7927.
- [11] M. S. T. Roudier, "Photospheric downflows observed with SDO/HMI, HINODE, and an MHD simulation," *Astron. Astrophys.*, vol. 647, 2021, doi: 10.1051/0004-6361/202040172.
- [12] R. K. Snodgrass, H. B., & Ulrich, "Rotation measurements and cross-correlation methods," *Astrophys. J.*, vol. 351, pp. 309–316, 1990, doi: https://doi.org/10.1086/168467.
- [13] D. Permata, S. M., & Herdiwijaya, "Sunspot tracking and solar rotation using SDO/HMI data," *J. Phys. Conf. Ser.*, vol. 1204, 2019, doi: https://doi.org/10.1088/1742-6596/1204/1/012095.
- [14] C. Webb, J. K., Carswell, R. F., & Lee, "Accurate Voigt profile fitting and model selection," *Astron. Astrophys.*, vol. 647, p. A7, 2021, doi: https://doi.org/10.1051/0004-6361/202039876.
- [15] K. Hotta, H., & Kusano, "Magnetohydrodynamic simulations of solar differential rotation," *Nat. Astron.*, vol. 5, pp. 1100–1106, 2021, doi: https://doi.org/10.1038/s41550-021-01422-7.
- [16] X. Yan, "Normalization methods for solar flare spectroscopy: A comparative study," *Sol. Phys.*, vol. 300, no. 1, p. 45, 2025, doi: https://doi.org/10.1007/s11207-025-02388-9.
- [17] T. Hotta, H., Kusano, K., & Sekii, "Solar differential rotation maintained by magnetic fields and anisotropic turbulence," *Nat. Astron.*, vol. 6, pp. 832–839, 2022, doi: https://doi.org/10.1038/s41550-022-01638-4.
- [18] R. C. Carrington, "On the Distribution of the Solar Spots in Latitude since the Beginning of the Year 1854; with a Map," *Mon. Not. R. Astron. Soc.*, vol. 19, no. 1, pp. 1–3, 1858, doi: https://doi.org/10.1093/mnras/19.1.1a.
- [19] P. Garaud, "Latitudinal shear instability in the solar tachocline," *Mon. Not. R. Astron. Soc.*, vol. 324, no. 1, pp. 68–76, 2001, doi: https://doi.org/10.1046/j.1365-8711.2001.04245.x.
- [20] François Rincon & Michel Rieutord, "The Sun's supergranulation," *Living Rev. Sol. Phys.*, vol. 15, no. 6, 2018, doi: https://doi.org/10.1007/s41116-018-0013-5.
- [21] and A. G. Abhishek Rajhans, Durgesh Tripathi, Vinay L. Kashyap, James A. Klimchuk, "Center-to-limb Variation of Transition-region Doppler Shifts in Active Regions," *Astrophys. J.*, vol. 944, no. 2, 2023, doi: 10.3847/1538-4357/acb4ed.
- [22] D. Vargas, A., Smith, J., Patel, R., & Lin, "Comparative evaluation of continuum-fitting strategies for astrophysical spectra," *J. Astron. Instrum.*, vol. 13, no. 1, p. 2450002, 2024, doi: https://doi.org/10.1142/S2251171724500021.
- [23] J. F. M. Cretignier, "RASSINE: Interactive tool for normalising stellar spectra," *Astron. Astrophys.*, vol. 640, 2020, doi: https://doi.org/10.1051/0004-6361/202037722.
- [24] P. P. M. Koleva, "ULySS: a full spectrum fitting package," *Astron. Astrophys.*, vol. 501, no. 3, pp. 1269–1279, 2009, doi: https://doi.org/10.1051/0004-6361/200811467.
- [25] P. F. M. Scodeggio, "The VVDS Data-Reduction Pipeline: Introducing VIPGI, the VIMOS Interactive Pipeline and Graphical Interface," *Publ. Astron. Soc. Pacific*, vol. 117, no. 837, 2005, doi: 10.1086/496937.
- [26] J.-K. Krogager, "VoigtFit: A Python package for Voigt profile fitting," *Astron. Comput.*, vol. 23, pp. 1–11, 2018, doi: https://doi.org/10.1016/j.ascom.2018.02.004.
- [27] T. T. García, "Voigt profile fitting to quasar absorption lines: an analytic approximation to the Voigt–Hjerting function," *Mon. Not. R. Astron. Soc.*, vol. 369, no. 4, pp. 2025–2035, 2006, doi: https://doi.org/10.1111/j.1365-2966.2006.10450.x.

- [28] A. Liang, C., & Kravtsov, "Bayesian Voigt profile fitting with affine-invariant MCMC," *J. Open Source Softw.*, vol. 2, no. 18, p. 336, 2017, doi: https://doi.org/10.21105/joss.00336.
- [29] R. Fenning, S. MacHida, D. Kelliher, A. Khan, and R. Edgecock, "High-order dispersion suppression for FFAG-based optics," J. Instrum., vol. 7, no. 05, p. P05011, May 2012, doi: 10.1088/1748-0221/7/05/P05011.
- [30] V. V. Makarov, "Modeling solar velocity fields from Doppler measurements," *Astrophys. J.*, vol. 715, no. 1, pp. 265–275, 2010, doi: https://doi.org/10.1088/0004-637X/715/1/265.
- [31] M. de la Cruz Rodríguez, J., Kiselman, D., & Carlsson, "Absolute velocity references for solar observations from 3D simulations," *Astron. Astrophys.*, vol. 528, 2011, doi: https://doi.org/10.1051/0004-6361/201015217.
- [32] A. A. N. & P. H. S. S. Couvidat, J. Schou, J. T. Hoeksema, R. S. Bogart, R. I. Bush, T. L. Duvall Jr., Y. Liu, "Observables Processing for the Helioseismic and Magnetic Imager Instrument on the Solar Dynamics Observatory," *Sol. Phys.*, vol. 291, pp. 1887–1938, 2016, doi: https://doi.org/10.1007/s11207-016-0957-3.
- [33] H. Pal, P. S., Steinegger, M., Arlt, R., Denker, C., & Balthasar, "Digitized full-disk solar plates from the Einstein Tower (1943–1991): Calibration and access," *Sol. Phys.*, vol. 295, no. 6, p. 87, 2020, doi: https://doi.org/10.1007/s11207-020-01656-y.
- [34] F. Ermolli, I., Giorgi, F., Romano, P., Stangalini, M., Vecchio, A., & Zuccarello, "Rome/PSPT full-disk solar observations: Data and applications," *Sol. Phys.*, vol. 297, no. 6, p. 87, 2022, doi: https://doi.org/10.1007/s11207-022-02021-6.
- [35] C. Xu, Z., Li, H., & Fang, "Spectroscopic diagnostics of solar plasma velocities," *Astron. Astrophys.*, vol. 664, 2022, doi: https://doi.org/10.1051/0004-6361/202243210.
- [36] H. P. Brooks, D. H., Ugarte-Urra, I., & Warren, "Full-Sun coronal Doppler velocity maps with EIS," *Astrophys. J.*, vol. 799, no. 2, p. 70, 2015, doi: https://doi.org/10.1088/0004-637X/799/2/70.
- [37] I. S. D. Sudar, "Steps towards a high precision solar rotation profile: Results from SDO/AIA coronal bright point data," *Astron. Astrophys.*, vol. 575, 2015, [Online]. Available: https://www.aanda.org/articles/aa/full_html/2015/03/aa24929-14/aa24929-14.html
- [38] M. D. Zdenek Hrazdíra, "Iterative Phase Correlation Algorithm for High-precision Subpixel Image Registration," *Astrophys. J. Suppl. Ser.*, vol. 247, no. 1, p. 8, 2020, doi: 10.3847/1538-4365/ab63d7.
- [39] H. M. A. Lekshmi B, Dibyendu Nandy, "Asymmetry in Solar Torsional Oscillation and the Sunspot Cycle," *Astrophys. J.*, vol. 86, no. 121, 2018, [Online]. Available: https://iopscience.iop.org/article/10.3847/1538-4357/aacbd5/pdf
- [40] J. Z. Alexander V. Getling, Alexander G. Kosovichev, "Evolution of Subsurface Zonal and Meridional Flows in Solar Cycle 24 from Helioseismological Data," *Astrophys. J. Lett.*, vol. 908, no. 2, 2021, doi: https://doi.org/10.48550/arXiv.2012.15555.
- [41] M. S. T. Roudier, "Large-scale photospheric motions determined from granule tracking and helioseismology from SDO/HMI data," *Astron. Astrophys.*, vol. 611, 2018, doi: https://doi.org/10.1051/0004-6361/201732014.
- [42] R. J.-Ś. I. Poljančić Beljan, "Solar differential rotation in the period 1964–2016 determined by the Kanzelhöhe data set," *Astron. Astrophys.*, vol. 606, 2017, doi: https://doi.org/10.1051/0004-6361/201731047.
- [43] S. F. C. Stewart, "Effects of transducer, velocity, Doppler angle, and instrument settings on the accuracy of color Doppler ultrasound," *Ultrasound Med. Biol.*, vol. 27,



- no. 4, pp. 551–64, 2001, doi: 10.1016/S0301-5629(01)00357-X.
- [44] T. Schöll, M., Egidi, A., & Dudok de Wit, "Processing challenges in solar irradiance composites (SOLID)," *Sol. Phys.*, vol. 291, no. 1, pp. 159–177, 2016, doi: https://doi.org/10.1007/s11207-015-0830-2.
- [45] H. B. Snodgrass, "Solar differential rotation from magnetic features," *Astrophys. J.*, vol. 270, pp. 288–299, 1983, doi: https://doi.org/10.1086/161124.
- [46] R. Howe *et al.*, "Large-scale zonal flows near the solar surface: A comparison of results from local and global helioseismology with direct doppler measurements," *Sol. Phys.*, vol. 235, no. 1–2, pp. 1–15, 2006, doi: 10.1007/S11207-006-0117-2.
- [47] E. B. Zuhal Er, "Dual axis solar angle tracking system without any sensor," *J. Energy Syst.*, vol. 2, no. 3, pp. 130–139, 2018, doi: 10.30521/jes.456606.
- [48] S. Routh, "Image-correlation-based solar flow mapping," *Sol. Phys.*, 2024, doi: https://doi.org/10.1007/s11207-024-02189-1.
- [49] Z.-C. L. and L. Gizon, "Doppler velocity of m=1 high-latitude inertial mode over the last five sunspot cycles," *arXiv:2409.06896v2*, 2025, [Online]. Available: https://arxiv.org/html/2409.06896v2



Copyright © by authors and 50Sea. This work is licensed under the Creative Commons Attribution 4.0 International License.